Assessment of the two relaxation time Lattice-Boltzmann scheme to simulate Stokes flow in porous media

L. Talon,[1] D. Bauer,[2] N. Gland,[2] S. Youssef,[2] H. Auradou,[1] and I. Ginzburg[3]

Received 12 September 2011; revised 29 February 2012; accepted 18 March 2012; published 24 April 2012.

[1] The recent advances in 3-D imaging of porous structures have generated a tremendous interest in the simulation of complex single and two-phase flows. Lattice-Boltzmann (LB) schemes present a powerful tool to solve the flow field directly from the binarized 3-D images. However, as viscosity often plays an important role, the LB scheme should correctly treat viscosity effects. This is the case using a LB scheme with two relaxation times (TRT) unlike the broadly used, the single-relaxation rate, BGK, where the velocity of the modeled fluid does not vary as the inverse of the viscosity applying the bounce-back (no-slip) boundary rule. The aim of this work is to apply the LB-TRT approach to different types of porous media (straight channels, 2-D model porous media, sandstone) to solve for the flow field and to evaluate the approach in terms of parameter dependence, error and convergence time on the basis of permeability. We show that the variation of permeability with the free relaxation parameter Λ of the TRT scheme depends on the heterogeneity of the sample and on the numerical resolution. The convergence time depends on the applied viscosity and the parameter standing for the speed of sound, thus the computation time can be reduced by choosing appropriate values of those parameters. Two approaches to calculate permeability (Darcy's law and viscous energy dissipation) are proposed and investigated. We recommend to use Darcy's law, as dependence on Λ is less important. Periodic (in the presence of a driving body force) and pressure boundary conditions are evaluated in terms of the results.

Citation: Talon, L., D. Bauer, N. Gland, S. Youssef, H. Auradou, and I. Ginzburg (2012), Assessment of the two relaxation time Lattice-Boltzmann scheme to simulate Stokes flow in porous media, *Water Resour. Res.*, *48*, W04526, doi:10.1029/2011WR011385.

1. Introduction

[2] Since the past decade, numerical experiments are commonly performed to determine and investigate transport properties of porous structures such as electrical conductivity, permeability, solute dispersion, relative displacement of a two-phase flow or NMR response. A better understanding of physical processes, and their complex interplay with the pore structure, is nowadays achieved by solving the governing equations directly in the pore space obtained from microtomographic (micro-CT) images [*Auzerais et al.*, 1996; *Arns et al.*, 2001, 2004; *Talabi et al.*, 2009; *Zhan et al.*, 2010; *Ovaysi and Piri*, 2010; *Bauer et al.*, 2011]. The improvement and development of such approach is important, for instance in geophysics, to understand the interaction between the rock and the fluids and the resulting consequences on the transport behavior. In contaminant hydrology and in petroleum engineering, the method permits the determination of the (relative) permeabilities of rocks and provides a fundamental understanding of the dispersion process at the pore level.

[3] Most of the past studies deal with the flow of incompressible viscous fluids and various numerical methods to solve the flow equations were proposed. Two distinct approaches should be mentioned: Pore network models [e.g., *Fatt*, 1956; *Joekar-Niasar and Hassanizadeh*, 2011] and direct numerical simulations (e.g., Finite Element [*Borne*, 1992; *Sun et al.*, 2010], Finite Volume [*Adler et al.*, 1990; *Mostaghimi et al.*, 2010], Lattice-Boltzmann [*Cancelliere*, 1990; *Zaretskiy et al.*, 2010]). The first is based on the modeling of the pore space by a network of interconnected pores and throats, reducing the governing equations to a system of linear equations, which can be easily solved. The second uses the voxel representation of the pore space obtained from the micro-CT images as numerical grid without major modification of the rock geometry and topology. Lately, Lattice-Boltzmann schemes became very popular. The reason for this lies mainly in the simplicity to solve the flow in complex geometries like porous media. In addition, Lattice-Boltzmann schemes are easily parallelized and therefore ideally suited to treat relatively large volumes. This technique was developed following the pioneering works of *Rothman* [1988] on Lattice Gas Automata (LGA) and *Succi et al.* [1989] on Lattice-Boltzmann Equation (LBE). Among the different schemes, the BGK model [*Qian et al.*, 1992] with a single-relaxation parameter τ in combination with the bounce-back boundary rule is the most popular. A major drawback of the method is that the fluid velocity is not proportional to the inverse of its viscosity. As a consequence,

[1]Laboratoire FAST, UMR CNRS 7608, Universités Paris VI et Paris XI, Orsay, France.
[2]IFP Energies nouvelles, Rueil-Malmaison, France.
[3]Antony Regional Centre, HBAN, Cemagref/Irstea, Antony, France.

Copyright 2012 by the American Geophysical Union
0043-1397/12/2011WR011385

the permeability obtained with this method varies with the viscosity. This dependence is mainly due to the bounce-back boundary rule that imposes the location of the solid boundary which has a numerical error that depends on the viscosity. To overcome this problem, one solution is to use a more precise boundary scheme [*Ginzburg and d'Humières*, 2003; *Ginzburg et al.*, 2008a] or to increase the resolution of the numerical domain, e.g., the pore space. Yet, imaging techniques including micro-CT have a finite resolution that can be of the same order as the pore size, making this approach inappropriate. Another solution proposed by *Manwart et al.* [2002] is to use a "magic" viscosity that corresponds to the value of the relaxation time ($\tau \sim 0.6$) at which the effective permeability does not depend on the resolution of the numerical domain. Yet, this procedure has two disadvantages. First, the prescribed τ depends on the porous structure [*Ginzburg and d'Humières*, 2003], the value obtained for Fontainebleau sandstone might not be the same for other media. Second, since the viscosity is imposed, this procedure cannot be used in the case of two phase flow with different viscosities or non-Newtonian flow. Such situations are however encountered in many applications such as in Enhanced Oil Recovery [*Wu and Pruess*, 1996] as well as in soil remediation. A possible solution is to improve the BGK model by using a multiple-relaxation-time (MRT) model [*d'Humières et al.*, 2002] or a two-relaxation-time (TRT) model [*Ginzburg*, 2007]. The ability of the MRT and TRT schemes were tested on synthetic model structures like fiber materials [*Ginzburg and d'Humières*, 2003], body-centered cubic arrays of spheres and random-sized sphere packings [*Pan et al.*, 2006] and for several other regular structures using the TRT model [*Ginzburg et al.*, 2008b]. As demonstrated analytically in the work of *d'Humières and Ginzburg* [2009], MRT schemes lead to viscosity independent results only if the free relaxation parameters are correctly chosen. The proper choice should keep fixed the specific combinations Λ (defined in section 2) for all symmetric and antisymmetric collision modes. The TRT scheme is the most efficient operator for low Reynolds number flow. However, improper choice of the free relaxation parameter in the MRT scheme leads to viscosity-dependent permeability, explaining the result of *Narvaez et al.* [2010]. It is important to remark that even if the MRT, in its more general form, might be less efficient in terms of computational cost, this is not the case for the TRT scheme where computational costs equal those of BGK.

[4] Many articles on porous media apply the Navier-Stokes equilibrium (and assuming low Reynolds number). We will use Stokes equilibrium that is simpler and sufficient for our purpose. The goal of the present paper is to assess the TRT scheme to solve Stokes flow for pressure P and momentum $\vec{j}$, prescribing kinematic viscosity ν and external body forcing $\rho_0\vec{F}$:

$$\vec{\nabla}P - \rho_0\vec{F} = \nu\Delta\vec{j}, \tag{1}$$

in different types of porous media (straight channels, 2-D generated porous media and binarized 3-D images of Fontainebleau sandstone). The emphasis will on the evaluation of the scheme in terms of parameter dependence, errors and convergence time on the basis of permeability. The structure of the paper is as follows: the numerical implementation is presented in section 2. In section 3, we present the results obtained from the different configurations. Section 4 is dedicated to the summary and conclusions. In Appendix A, we show how to compute the effective permeability from the viscous energy dissipation.

2. Hydrodynamic Problem and Presentation of the TRT Method

2.1. Description of the TRT Method

[5] As a matter of principle, the basic idea of the Lattice-Boltzmann method is to discretize the velocity distribution function of particles on a grid. To this goal, we introduce the population f_q as the density of particles moving with the velocity $\vec{c}_q$. The algorithm is mainly a succession of two steps. The first is the propagation step (equation (2)), where we move the density on the grid according to its velocity. The second is the collision step (equation (3)), where we redistribute populations meeting at the same node using a collision operator that depends on the local macroscopic quantities (pressure, momentum, ...).

[6] Modeling of the Navier-Stokes equations with the TRT operator is discussed in detail in [*Ginzburg*, 2007; *Ginzburg et al.*, 2008a; *Ginzburg*, 2008]. In the present work, we use the D3Q19 Stokes scheme where the unknown variable of the scheme at time t is the Q-dimensional population vector $\{f_q, q = 0, \ldots, Q_m\}$, specified on the nodes $\vec{r}$ of the D-dimensional regular computational mesh Ω, where $Q_m = Q - 1 = 18$ and $D = 3$.

[7] The nodes of the grid are related by the velocity vectors $\vec{c}_q$, $q = 1, \ldots, Q_m$ and $\vec{c}_0 \equiv 0$. Without loss of generality, we assume that the first $\frac{Q_m}{2}$ vectors $\vec{c}_q$ are opposite to the second set of $\frac{Q_m}{2}$ vectors defined as $\vec{c}_{\bar{q}} = -\vec{c}_q$. We then operate with the symmetric $\{f_q^+ = (f_q + f_{\bar{q}})/2\}$ and the antisymmetric $\{f_q^- = (f_q - f_{\bar{q}})/2\})$ components, $q = 1, \ldots, Q_m/2$. We set $f_0^+ = f_0$ and $f_0^- = 0$ for immobile population. The two-relaxation-times (TRT) update is performed with the prescribed equilibrium distribution $\{e_q^\pm\}$, the external momentum quantity S_q^- and two collision eigenvalues $s^\pm \in]0, 2[$, s^+ for all symmetric and s^- for all antisymmetric nonequilibrium components, $\{n_q^+\}$ and $\{n_q^-\}$, respectively. Thus, we obtain

$$\begin{aligned} f_0(\vec{r}, t+1) &= [f_0(1-s^+) + s^+ e_0](\vec{r}, t), f_q(\vec{r} + \vec{c}_q, t+1) \\ &= \tilde{f}_q(\vec{r}, t), \end{aligned} \tag{2}$$

with

$$\begin{aligned} \tilde{f}_q(\vec{r}, t) &= [f_q - s^+ n_q^+ - s^- n_q^- + S_q^-](\vec{r}, t), q = 1, \ldots, \frac{Q_m}{2} \\ \tilde{f}_{\bar{q}}(\vec{r}, t) &= [f_{\bar{q}} - s^+ n_q^+ + s^- n_q^- - S_q^-](\vec{r}, t), q = 1, \ldots, \frac{Q_m}{2}, \end{aligned} \tag{3}$$

where

$$\begin{aligned} &n_q^\pm = \left(f_q^\pm - e_q^\pm\right), f_q^\pm = \frac{1}{2}\left(f_q \pm f_{\bar{q}}\right), \\ &\text{when } \vec{c}_{\bar{q}} = -\vec{c}_q,\ q = 1, \ldots, \frac{Q_m}{2}. \end{aligned} \tag{4}$$

[8] Computing the linear collision operator we have accounted that the symmetric components are the same for two opposite populations, and hence $f_q^+ = f_{\overline{q}}^+$, $n_q^+ = n_{\overline{q}}^+$, while the antisymmetric components have the opposite signs, and hence $f_q^- = -f_{\overline{q}}^-$, $n_q^- = -n_{\overline{q}}^-$.

[9] The fluid dynamics, with the presence of a body force $\rho_0\vec{F}$, are obtained by prescribing the external momentum set of quantities $\{S_q^-\}$ and the equilibrium functions $e_q^{\pm}$. The latter require the computation of two quantities: the local mass

$$\rho = \sum_{q=0}^{Q_m} f_q = f_0 + 2\sum_{q=1}^{Q_m/2} f_q^+, \tag{5}$$

and local momentum

$$\vec{J} = \sum_{q=1}^{Q_m} f_q \vec{c}_q = 2\sum_{q=1}^{Q_m/2} f_q^- \vec{c}_q. \tag{6}$$

Equilibrium functions then become

$$e_q^+ = c_s^2 t_q^\star \rho,\ e_q^- = t_q^\star(\vec{J}\cdot\vec{c}_q),\ e_0 = \rho - 2\sum_{q=1}^{Q_m/2} e_q^+ \tag{7}$$

with

$$S_q^- = t_q^\star \rho_0 \vec{F}\cdot\vec{c}_q, \tag{8}$$

where ρ_0 is a constant and taken as the initial mass average of the fluid (routinely, ρ_0 equals 1) and the weights $\{t_q^\star\}$ are isotropic and obey two constraints:

$$\sum_q t_q^\star c_{q\alpha} c_{q\beta} = \delta_{\alpha\beta},\ \forall\alpha,\beta \quad \text{and} \quad \sum_q t_q^\star c_{q\alpha}^2 c_{q\beta}^2 = \frac{1}{3},\ \forall\alpha\neq\beta. \tag{9}$$

Here, they take the value $t_q^\star = \{t^I, t^{II}\} = \left\{\frac{1}{6}, \frac{1}{12}\right\}$ for, respectively, the first and second (diagonal) neighbor link in the D3Q19 model. We remark that the classical BGK model is recovered when $s^+ = s^- = \frac{1}{\tau}$.

[10] The TRT scheme with equilibrium functions (7)–(9) models solutions to Stokes equations (in lattice units) by

$$\partial_t\rho + \vec{\nabla}\cdot\vec{j} = 0, \partial_t\vec{j} + \vec{\nabla}P - \rho_0\vec{F} = \nu\Delta\vec{j} \tag{10}$$

where the kinematic viscosity is given by $\nu = \frac{1}{3}\left(\frac{1}{s^+} - \frac{1}{2}\right)$, the pressure P by $P = c_s^2\rho$ and the macroscopic momentum by: $\vec{j} = \vec{J} + \frac{1}{2}\rho_0\vec{F}$ with $\vec{u} = \vec{j}/\rho_0$. With this definition, the average velocity and mass flux are equal [*Ginzburg and d'Humières*, 2003] which is important—as we shall see—for the permeability computations.

[11] The sound velocity c_s is a tunable positive parameter, $c_s^2 < c_s^{2max} < 1$, which is usually set to $\sqrt{1/3}$, [*Lallemand and Luo*, 2000]. Nonnegativity of the immobile weight e_0/ρ imposes $c_s^{2max} = \frac{1}{2}$ for the D3Q19. However in the present computation we reached $c_s^{2max} \approx 0.6$ without affecting the results. This agrees with the stability analysis [*Ginzburg*, 2012] where necessary stability condition for D3Q19 is $c_s^2 < 1/(1+2t^I) = 3/4$.

[12] In the TRT scheme, the second eigenvalue s^- is a free parameter (we recall that $s^- \in]0,2[$). In addition, for a steady flow, it has been recently demonstrated in the work of *Ginzburg et al.* [2008a] and *d'Humières and Ginzburg* [2009] that $\vec{j}$ varies as the inverse of ν, only if the associated parameter $\Lambda = (\frac{1}{s^+} - \frac{1}{2})(\frac{1}{s^-} - \frac{1}{2})$ is kept constant. Consequently, we will hereafter use Λ as control parameter rather than s^-. We note that in the case of the standard BGK scheme, we have $s^- = s^+ = 1/\tau$ and thus: $\Lambda_{BGK} = 9\nu^2$.

2.2. Boundary Conditions

[13] In LB simulations, no-slip boundary conditions, i.e., $\vec{j}(\vec{x}) = \vec{0}$ at the solid/fluid interface are implemented by the so-called bounce-back rule. In this method, particles meeting a solid perform a bounce back rule such that: $f_{\overline{q}}(\vec{r}, t+1) = \tilde{f}_q(\vec{r}, t)$. This rule imposes the position of the solid interface half way between the two grid points located in the fluid and in the solid for a straight velocity profile. Other methods do exist to define the interface position. Yet, for micro-CT images the position of the interface is not precisely known since it depends on the resolution and segmentation procedure applied to separate the void from the solid space (see section 3.4); we thus solely considered the bounce back rule in the present study. Another advantage of this rule is to keep the linearity of Stokes flow when Λ is fixed.

[14] In order to drive the fluid, several methods exist [*Succi*, 2001]. One is to impose a uniform body force in the fluid at every point according to the definition of $\vec{F}$ in equation (10), similar to a gravitational body force acting on the fluid. This method is broadly used due to its relatively simple implementation, however, it requires a periodic sample. This condition can be limiting in the case of 3-D natural porous media since making the domain periodic implies an increase of the domain by a factor 2 per axis and hence an increase of the memory and computational time (for example, a rough estimation of the memory requirement of a volume of size N^3 voxel with a porosity of ϕ is given by around $\sim 160N^3\phi$ bytes). One may mimic the periodic domain replacing periodic conditions by specular reflexion on its bounds. This technique requires however a careful preprogramming of link connections in complicated local geometries, such as the corners.

[15] Another possible boundary condition consists of the application of a pressure difference between the inlet and the outlet of the system (here the plane $x = 0$ and $x = L$, respectively). Numerically, the boundary pressure and a zero tangential velocity at the inlet and outlet are imposed by using a simplified mixed antibounce back method inspired from [*Ginzburg et al.*, 2008b] (see equation (2.41)):

$$\begin{aligned} f_{\overline{q}}(\vec{r}, t+1) = -\tilde{f}_q(\vec{r}, t) + 2t_q^\star P_0 - \left(1 - \frac{2}{s^+}\right)s^+ n_q^+(\vec{r}, t) \\ + \frac{1}{2}t_q^\star c_{qy} j_y(\vec{r}, t) + \frac{1}{2}t_q^\star c_{qz} j_z(\vec{r}, t), \end{aligned} \tag{11}$$

where P_0 is the imposed pressure and q is the link that crosses the boundary, $\tilde{f}_q(\vec{r}, t)$ is thus the outgoing distribution after collision. We remark that the last two terms of

equation (11) forcing $j_y = j_z = 0$ do not affect significantly the permeability calculation; they are however useful to remove numerical oscillations observed at the boundary. Their weights can be tuned by changing the prefactor which is kept constant and equal to $1/2$ in the present work. Both driving condition types are used in this study. We refer in the following as DC1: body force, periodic in the direction of flow, no flow on the borders in the other directions, DC2: pressure gradient in the direction of flow, no flow on the borders in the other directions. In both cases, we used the bounce back rule at the solid-fluid interface.

2.3. Determination of the Permeability

[16] The macroscopic permeability is computed from the solution of the hydrodynamic problem (equation (1)) in two ways. The first uses Darcy's law which relates the average local velocity to the average pressure gradient. The diagonal elements of the permeability tensor **K** can be computed as

$$K_{D,ii} = -\frac{\nu < j_i(\vec{x}) >}{< \nabla_i P - \rho_0 \vec{F}_i >}, i = 1,2,3, \tag{12}$$

where $< j_i(\vec{x}) >$ is the volume averaged ith component of the velocity field, and $< \nabla_i P - \rho_0 \vec{F}_i >$ is the ith component of the applied driving force across the sample. In the case of a periodic structure, $< \nabla_i P > = 0$ and $\rho_0 \vec{F}_i$ is the volume averaged value of the applied forcing (see *Ginzburg and d'Humières* [2003] for details). When the pressure gradient is prescribed, then $< \nabla_i P >$ is computed from the average pressure at the inlet and the average pressure at the outlet.

[17] The second method is to consider energy dissipation due to viscous drag [*Happel and Brenner*, 1983]. In this case, the permeability is computed using the following relation

$$K_{E,ii} = \frac{< j_i(\vec{x}) >^2}{2 < \Delta(\vec{j}) : \Delta(\vec{j}) >}, \tag{13}$$

where $\Delta(\vec{x})$ is the symmetric deformation rate tensor given by

$$\Delta_{ij} = \frac{1}{2}\left(\frac{\partial j_i}{\partial x_j} + \frac{\partial j_j}{\partial x_i}\right) \tag{14}$$

$$\Delta : \Delta = \frac{1}{2}\sum_{ij}\left[\left(\frac{\partial j_i}{\partial x_j}\right)^2 + \frac{\partial j_i}{\partial x_j}\frac{\partial j_j}{\partial x_i}\right]. \tag{15}$$

The main advantage in the second approach lies in the fact that LB scheme directly provide the deformation rate tensor. It is directly computed from the n_q^+ distribution using weight relation (9) as

$$\Delta_{ij}(\vec{j}) = -\frac{3s^+}{2}\sum_{q=1}^{Q_m} n_q^+ c_{qi} c_{qj}. \tag{16}$$

In the Appendix B, we show that the Darcy's law and energy dissipation approaches are identical for the driving conditions we have considered.

3. Results

[18] The principal interest of section 3 is to interpret the results obtained from binarized 3-D images of Fontainebleau sandstone and to provide recommendations and information on the choice of numerical parameters, permeability formulations and micro-CT resolution. Nevertheless, given the relatively complex structure of the sandstone, we first apply the LB-TRT scheme to simpler model structures (straight channel, assembly of straight channels in parallel or series, 2-D model porous media with different degrees of heterogeneity). These results will help us interpret the results obtained from the micro-CT images.

3.1. Flow in a Narrow Straight Channel

[19] In Appendix C, we show that permeabilities calculated either by Darcy's law (K_D) or by the energy dissipation approach (K_E) are in theory strictly identical. In section 3.1 we evaluate the influence of the resolution for both approaches by the TRT scheme using a simple geometry. To this goal we first present the *effective* TRT flow profile $j_x(y)$ as a function of Λ which is then used to determine analytically K_D and K_E. Then, we will investigate the dependence of the permeability on Λ by applying the simplest numerical integration rule (midpoint rue, corresponding to a summation) commonly used to average the values from the simulation data. Finally, we consider higher-order integration schemes.

[20] We first consider the flow in a channel consisting of two parallel plates with $D_{1/2}$ voxels filling the free space between the walls. The solid interfaces are assumed to be located half way between two adjacent voxels such that the bounce back condition is fulfilled at the first order. The effective profile computed by the TRT model assuming a body force $\rho_0 F_x$ follows a parabolic profile with,

$$j_x(y) = \frac{k_f}{2}\left(\left(\frac{D}{2}\right)^2 - y^2\right), \tag{17}$$

where $k_f = \frac{\rho_0 F_x}{\nu}$ and D is an effective width [*Ginzbourg and Adler*, 1994; *Ginzburg and d'Humières*, 2003] given by

$$D^2 = D_{1/2}^2 + \frac{16}{3}\Lambda - 1. \tag{18}$$

We see that the effective width (expressed in number of voxels) varies with Λ and equals the actual width when $\Lambda = 3/16$. This mismatch converges as $1/D_{1/2}^2$ but it may become important for low resolution when Λ is of the same order as $D_{1/2}^2$.

[21] We now investigate the influence of the numerical error on the permeability of the channel. For this geometry, the effective permeability K_D^{eff} calculated using the Darcy's law (see equation (12)) is

$$K_D^{eff} = \frac{< j_x >}{k_f}, \tag{19}$$

with

$$< j_x > = \frac{1}{2h}\int_{-h}^{h} j_x(y)dy = \frac{k_f D^2}{12}. \tag{20}$$

The effective permeability is thus related to the effective width by

$$K_D^{eff} = \frac{D^2}{12}. \tag{21}$$

The energy dissipation approach (see equation (13)) gives a permeability

$$K_E^{eff} = \frac{<j_x>^2}{2<\Delta^2>} \tag{22}$$

with

$$<\Delta^2> = \frac{1}{4h}\int_{-h}^{h}\left[\frac{\partial j_x}{\partial y}\right]^2 dy = -\frac{1}{4h}\int_{-h}^{h} j_x(y)\frac{\partial^2 j_x(y)}{\partial y^2}dy \tag{23}$$

or, using equation (17), we have $\frac{\partial^2 j_x(y)}{\partial y^2} = -k_f$ leading to

$$<\Delta^2> = \frac{{k_f}^2 D^2}{24} \tag{24}$$

so that equation (22) reduces to $K_E^{eff} = \frac{D^2}{12}$. Both approaches lead to the same value of the effective permeability using equation (18):

$$K^{eff} = K^{ex} + \frac{\frac{16}{3}\Lambda - 1}{12}, \text{ where } K^{ex} = \frac{D_{1/2}^2}{12}. \tag{25}$$

[22] The exact permeability is obtained for $\Lambda = 3/16$. However, to compute the permeabilities from the simulation data, integrals in equations (20) and (23) are replaced by sums. To investigate the influence of the numerical integration rule (midpoint rule, summation), we compute the mean averaged values from the effective solution:

$$\begin{aligned}
&<j_x>^{TH} = \frac{k_f}{n}\sum_{i=1}^{n}\left(h^2 - \left(i-\frac{1}{2}\right)^2\right) \text{ if } D_{1/2} = 2n,\\
&\Rightarrow <j_x>^{TH} = \frac{k_f}{2n+1}\left(2\sum_{i=1}^{n}(h^2 - i^2) + h^2\right) \text{ if } D_{1/2} = 2n+1,\\
&\text{then } <j_x>^{TH} = \frac{(3D^2 - D_{1/2}^2 + 1)k_f}{24}, D_{1/2} = 2n\\
&\text{or } \quad D_{1/2} = 2n+1.
\end{aligned} \tag{26}$$

and

$$\begin{aligned}
&<\Delta^2>^{TH} = \frac{k_f^2}{2n}\sum_{i=1}^{n}\left(i-\frac{1}{2}\right)^2 \text{ if } D_{1/2} = 2n\\
&\Rightarrow <\Delta^2>^{TH} = \frac{k_f^2}{(2n+1)}\sum_{i=1}^{n} i^2 \text{ if } D_{1/2} = 2n+1\\
&\text{then } <\Delta^2>^{TH} = \frac{k_f^2(D_{1/2}^2 - 1)}{24}, D_{1/2} = 2n \text{ or } D_{1/2} = 2n+1.
\end{aligned} \tag{27}$$

Note that relation (27) is exact since the first-order derivatives are computed exactly for the parabolic profile using equation (16). For Darcy's law, the discretization of equations (19) and (26) gives

$$K_D^{TH} = K^{ex} + \frac{8\Lambda - 1}{12}. \tag{28}$$

In this case numerical values are equal to the exact solution $K_D^{TH} = K^{ex}$ if $\Lambda = 1/8$.

[23] By means of the energy dissipation approach, equations (22), (26), and (27), yield

$$K_E^{TH} = \frac{(D_{1/2}^2 + 8\Lambda - 1)^2}{12(D_{1/2}^2 - 1)} \tag{29}$$

then $K_E^{TH} = K^{ex}$ if

$$\Lambda = \frac{1 - D_{1/2}^2 + \sqrt{D_{1/2}^2(D_{1/2}^2 - 1)}}{8}. \tag{30}$$

[24] Thus, for a given value of $D_{1/2}^2$ the exact permeability determined by the two approaches is obtained for two different values of Λ. The result is confirmed in Figure 1 which shows K_D^{TH}, K_E^{TH}, K_D^{TRT} and K_E^{TRT} normalized with K^{ex}. The numerical results completely agree with relations (28) and (29). Permeabilities computed by the Darcy's law or by the energy dissipation method using the TRT scheme coincide with the values predicted by the numerical analysis. In addition, they both show a linear increase with Λ and cross the normalized permeability of the channel $K = 1$ for two different values of Λ, $1/8$ and 0.0623, respectively. We can state that the slope of K_E^{TH} is higher for the energy dissipation method.

[25] Thus, although the exact permeability obtained by Darcy and by the energy dissipation approaches are identical using an exact integration rule, the simulation results differ due to the summation over the mesh. This difference plays an important role in a low resolved channel.

[26] However, replacing the midpoint rule by a trapezoidal rule, the "best" Λ value is $\Lambda = 5/16$ for Darcy's law and $\Lambda = \left[5 - 2D_{1/2}^2 + 2\sqrt{D_{1/2}^2(2 + D_{1/2}^2)}\right]/16$ for energy dissipation method (cf. equation (29) and (30) for midpoint rule). At the same time, applying the Simpson's rule, e.g., replacing $(h^2 - (i-1/2)^2)$ in the first line in equation (26) by $(h^2 - [(i-1)^2 + i^2 + 4(i-1/2)^2]/6)$, one obtains the following exact effective solution: $<j_x>^{TH} = (3D^2 - D_{1/2}^2)k_f/24$ which coincides with $K^{ex} = \frac{D_{1/2}}{12}$ when $D_{1/2} = D$, i.e., when $\Lambda = 3/16$. Similarly, Simpson's rule gives $<\Delta^2> = \frac{k_f D_{1/2}}{24}$, and then $K_E^{TH} = K^{ex}$ for $\Lambda = 3/16$. At this point we stress the Simpson's rule (S), midpoint (M) and trapezoidal (T) rules are related: $S = \frac{2M+T}{3}$. This relation is satisfied for Λ using Darcy's law: $\frac{3}{16} = \frac{1}{3}\left(2 \times \frac{1}{8} + \frac{5}{16}\right)$, because of the linearity of the effective width square with Λ. However, it is not so for the energy dissipation method computed as the ratio of two mean quantities. On this basis, we should expect less linear dependency on Λ for this method.

[27] Although one could suggest that a high-order integration method will also improve the precision in arbitrary

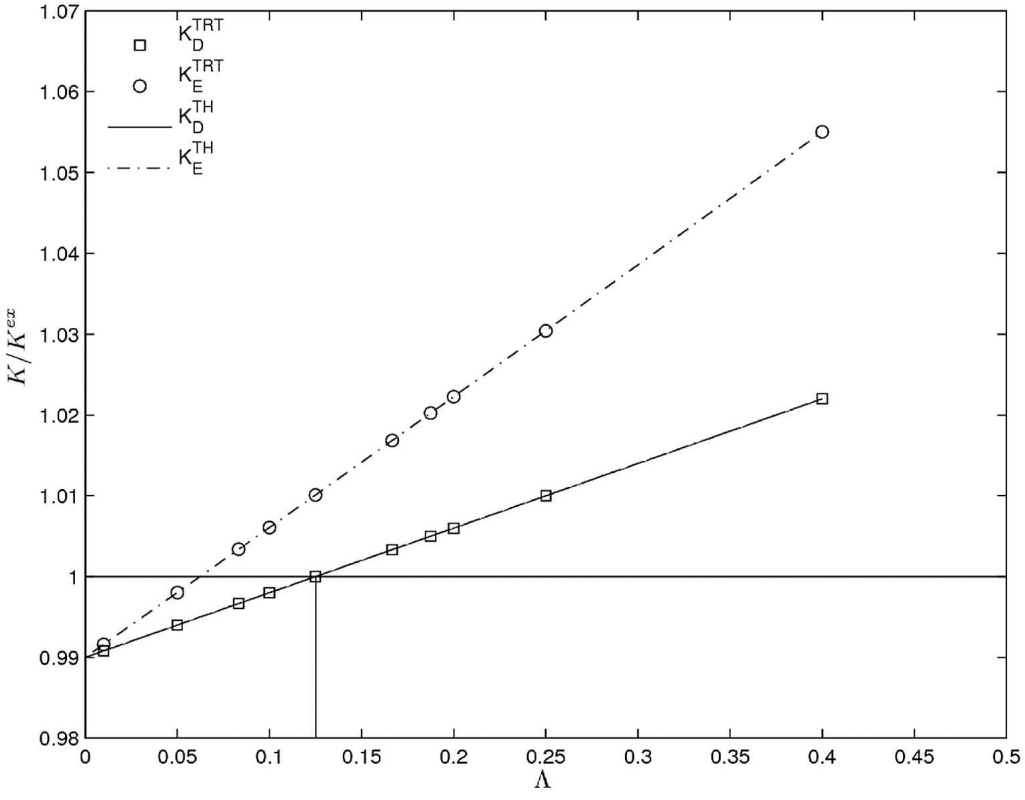

Figure 1. Permeability measured by the Darcy (squares) and the energy dissipation (circles) approaches for a channel of constant aperture $D_{1/2} = 10$ as a function of Λ. The two lines show the theoretical results given by equations (28) and (29).

geometry, we believe that it would be so only provided that (1) the effective solution imposes no-slip velocity at the boundary nodes with the effective local second-order precision, at least, and (2), one may perform accurate interpolations for the intermediate integration points. In porous media, it is difficult to reach the local second-order precision because of insufficient pore resolution and imprecise description of solid boundaries. At the same time, when the boundaries are precisely described, the higher-order accurate boundary schemes alone strongly reduce solution dependency on Λ [*Ginzburg and d'Humières*, 2003; *Ginzburg et al.*, 2008a]. They are the best candidates for most accurate permeability measurements, with or without using highly accurate integration rules.

3.2. Permeability of Independent Channels Placed in Parallel and Series

[28] To get insight into the sensitivity of Λ for a real porous media characterized by its topology and its degree of heterogeneity, we now consider a porous medium modeled by an ensemble of individual permeabilities placed in parallel or series with respect to the flow direction. The effective or macroscopic permeability, for the first case, is the arithmetic average of the individual permeabilities. For the second case, the effective permeability is given by the harmonic average. The individual permeabilities have a value corresponding to the one obtained by the TRT method and given by equation (28). The macroscopic permeability is thus also a function of Λ. To determine the influence of the degree of heterogeneity on the $K(\Lambda)$ curves, normalized permeabilities resulting from arithmetic and harmonic averages of the two normal random distributions of individual channel diameters with the same mean value: $< D_1 >=< D_2 >= 10$ and two standard deviations: $\sigma_1 = 1$, $\sigma_2 = 3.5$ are plotted in Figure 2 as a function of Λ.

[29] For the parallel configuration, the permeability varies linearly with Λ. However, for the second configuration, a negative curvature is observed. Also, the dependence on Λ is more pronounced for the distribution with the large standard deviation. This behavior can be explained by the so-called bottleneck effect. If a porous medium is characterized by a topology and heterogeneity in a way that it always allows the fluid to pass through large pores, global permeability and therefore dependency on Λ is determined by those highly resolved pores. Thus, in this case dependency on Λ is minor. However, in the case of a bottleneck system, where fluid is forced to pass through small restrictions, global system behavior depends on those underresolved regions [*Talon et al.*, 2010]. Thus, dependency on Λ becomes important and nonlinear.

3.3. Two-Dimensional Model Porous Media: Array of Circles and Truncated Gaussian Distribution

[30] Our attention is now drawn to the influence of viscosity by comparing the TRT to BGK scheme, the choice of driving conditions, the approach to determine permeability (Darcy: K_D or energy dissipation: K_E) and the convergence time as a function of the model parameters. To this goal, a regular and a random 2-D porous medium was generated. The first corresponds to an array of disks whereas

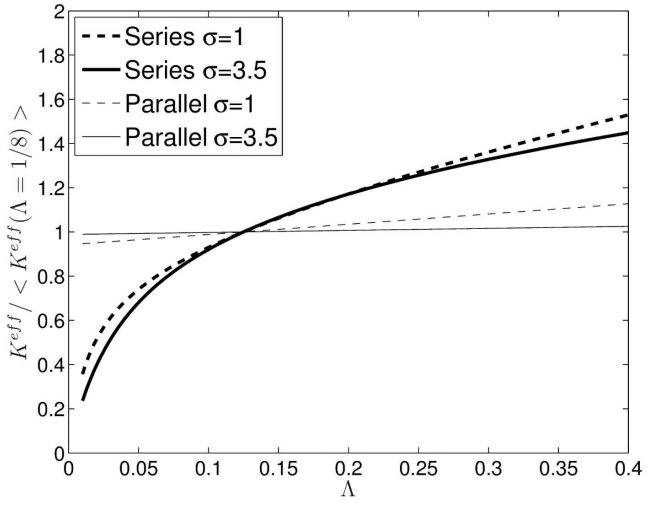

Figure 2. Macroscopic permeability values for straight channels acting in parallel (thin dashed and solid lines) or series (thick dashed and solid lines) normalized by $< K^{eff}(\Lambda = 1/8) >$. The diameters of the channels are randomly drawn from a normal distributions with a fixed mean $< D > = 10$ but two standard deviations $\sigma_1 = 1$ (dashed lines) and $\sigma_2 = 3.5$ (solid lines).

the second was generated by assigning random values taken from a Gaussian distribution to a two dimensional grid [*Adler et al.*, 1990]. All grid cells whose value is below a certain value c_{th} correspond to the solid phase and others to the void space. The value of c_{th} sets the porosity of the media to $1 - \phi = 0.5(1 + erf(c_{th}/\sqrt{2}))$. The two porous structures, displayed in Figure 3, have the same porosity, $\phi = 0.75$.

[31] Table 1 gives the permeability values obtained with TRT and BGK scheme for the random porous media. Results are given for both driving conditions (DC1: body force, DC2: pressure gradient). The values of the permeability obtained by TRT scheme are clearly viscosity independent whereas those determined by BGK do depend on ν. Table 1 also gives the permeability obtained with the different driving conditions (only for TRT scheme): the values are close demonstrating that conditions are equivalent. The small difference between the values can be explained by the size of the porous media, being periodic it is infinite for DC1, whereas for DC2 it has a finite size.

[32] Figure 4 shows the normalized permeability $\frac{K(\Lambda)}{K(\Lambda=0.1)}$ for the two porous media as a function of Λ. Values of Λ were chosen in the range of $\Lambda \in [0.01; 0.4]$, as $\Lambda = 3/8$ is the exact solution for diagonal Poiseuille flow. For higher values of Λ the error becomes very important (see *Ginzburg et al.* [2008b]). For both methods (Darcy's law or energy dissipation) and different porous structures, the permeability depends nonlinearly on Λ with a lower gradient for the regular network. This reduction can be explained by the above mentioned bottleneck effect (see section 3.2). In fact, the heterogeneous porous medium has a local distribution of the permeability which is larger than the one of the regular porous medium. Thus, bottleneck effect in the irregular porous media is more pronounced.

[33] Finally, the permeability increases faster with Λ when it is computed using the energy dissipation method as

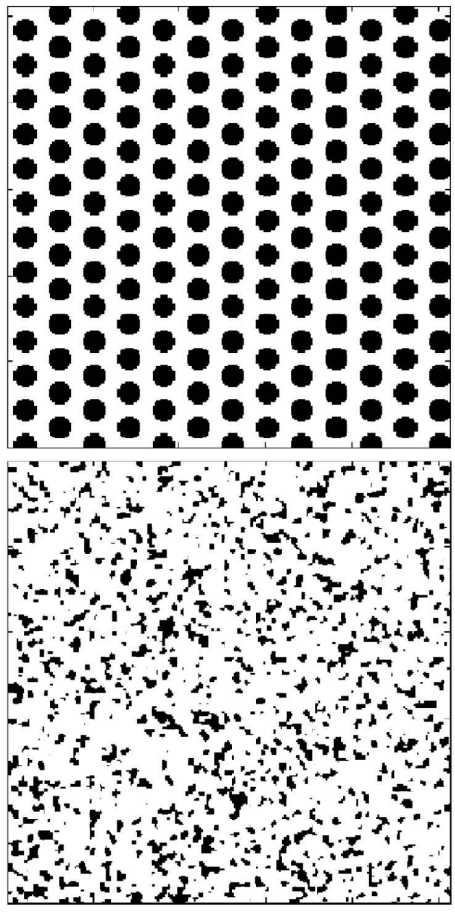

Figure 3. Regular and random 2-D model porous media where the black color represents the solid phase.

it is the case for a single channel. This increase is due to the computation of the ratio of two averaged quantities, $< j_x >$ and $< \Delta^2 >$, differently depending on Λ (see section 3.1) and, perhaps, to high-order errors in equation (16).

[34] Figure 5 (top left) shows the convergence of $K_D(t)$ toward its final value for different values of ν computed by the TRT scheme. Computations were done using the irregular porous medium. When a small value of ν is used, $K_D(t)$ converges with slight oscillations, they however become important for high values of ν. In order to determine the convergence time, we define criteria based upon the rate of change of the permeability $\left(\frac{\partial K(t)}{\partial t}, \text{ or numerically}, \frac{K(t_{i+1}) - K(t_i)}{t_{i+1} - t_i}\right)$. Criteria using the relative distance to the final value are not

Table 1. Permeability of the 2D Random Porous Media as a Function of the Viscosity and the Two Driving Conditions Calculated by the TRT and the BGK Methods[a]

	TRT: DC1		TRT: DC2		
Viscosity, ν	($\Lambda = 0.01$)	($\Lambda = 0.2$)	($\Lambda = 0.01$)	($\Lambda = 0.2$)	BGK: DC2
0.01	0.5986	0.8177	0.5942	0.8124	0.5308
0.05	0.5986	0.8177	0.5942	0.8124	0.6319
0.1	0.5986	0.8177	0.5942	0.8124	0.7282
0.2	0.5986	0.8177	0.5942	0.8124	0.8953
0.4	0.5986	0.8177	0.5942	0.8124	1.2002

[a]The two driving conditions were DC1 and DC2.

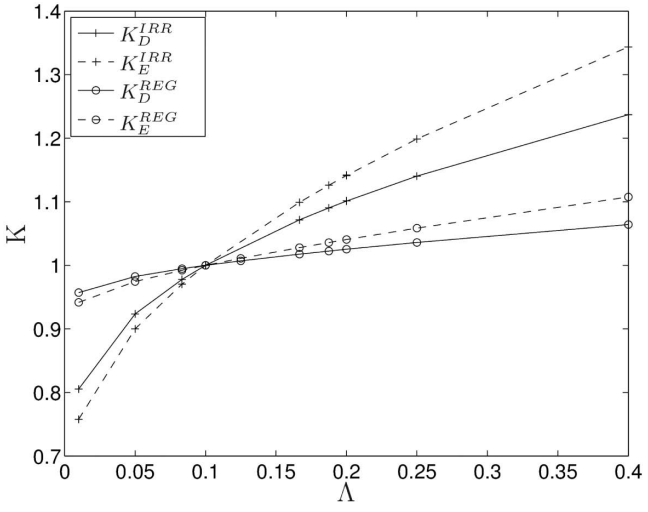

Figure 4. Normalized permeability $K(\Lambda)/K(\Lambda = 0.1)$ obtained for the random (crosses) and the regular (circles) 2-D porous media as a function of Λ calculated by the Darcy (solid line) and the energy dissipation approaches (dotted line).

suitable for natural porous media, since the exact permeability of the samples are often not known. In Figure 5 (top right) we plot $\frac{\partial K_D(t)}{\partial t}$ and we see that the convergence criteria is met after the last oscillation, once the rate of change is either below 10^{-10} (defined as criteria 1) or below 10^{-6} (defined as criteria 2). Figure 5 (bottom) shows convergence as well as its derivative for the BGK scheme. Convergence behavior is similar to that for the TRT scheme, indicating that it is mostly controlled by the viscosity value.

[35] Figure 6 gives the convergence time as a function of ν for the regular and the random porous media determined using the two criteria. As expected, the convergence time is shorter for criteria 2 than for criteria 1. The convergence time also varies with the fluid viscosity with a global minimum that depends on the porous structure and the applied criteria.

[36] As pointed out in section 2, the sound speed c_s is also a free parameter. Figure 7 shows the convergence time (criteria 2) as function of c_s^2 for various viscosities ν. We see that convergence time decreases with increasing values of c_s^2 and the dependence on viscosity becomes less important.

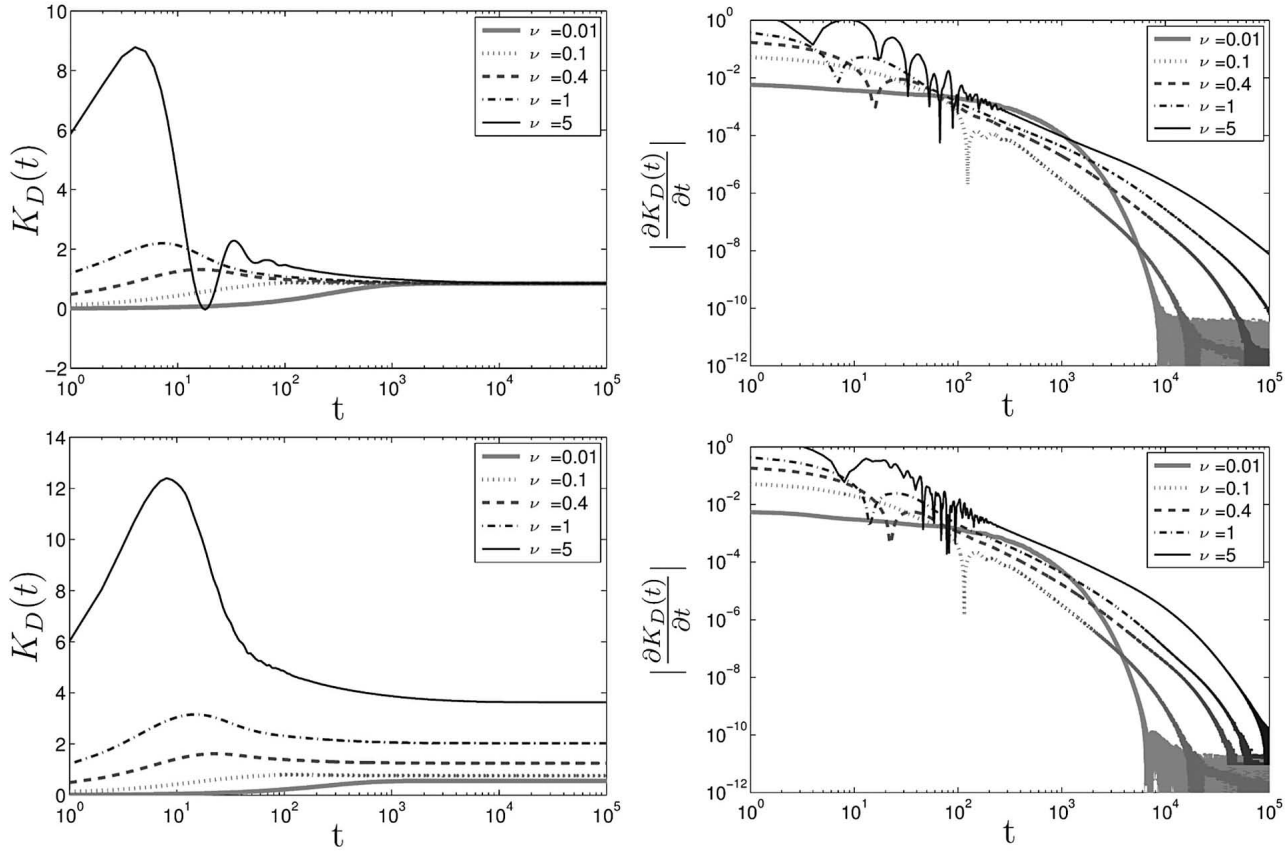

Figure 5. (left) Variation of the permeability $K(t)$ and (right) its derivative $\left|\frac{\partial K(t)}{\partial t}\right|$ as function of the number of iterations for different viscosities for the irregular porous media. (top) TRT simulations with $\Lambda = 0.2$. (bottom) BGK simulations.

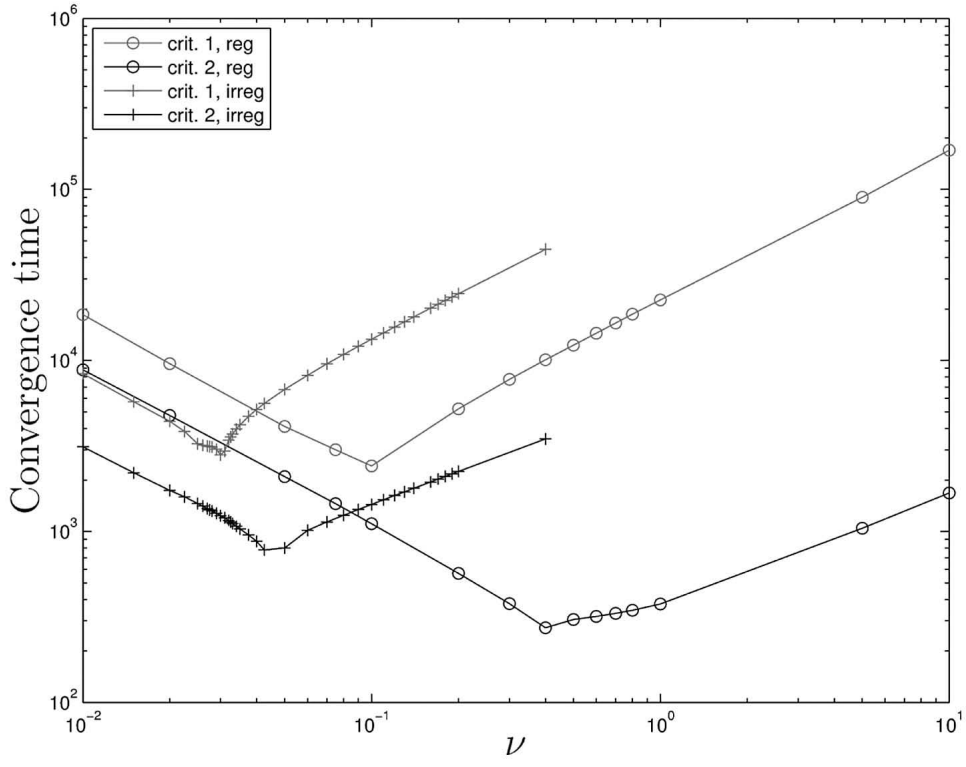

Figure 6. Convergence time as a function of the viscosity for the periodic (circles) and the random (crosses) porous media using criteria 1 (i.e., $|\frac{\partial K(t)}{\partial t}| < 10^{-10}$) (dotted lines) and criteria 2 (i.e., $|\frac{\partial K(t)}{\partial t}| < 10^{-6}$) (solid lines).

[37] As a consequence, the computation time may be optimized by using a proper combination of viscosity ν and speed of sound c_S. This behavior strongly depends on the porous structure. For instance, convergence time decreases with the viscosity in the case of Poiseuille flow (results not shown).

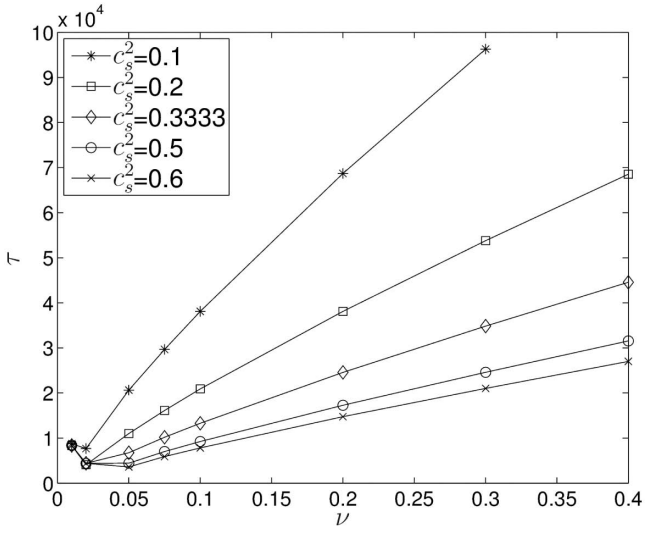

Figure 7. Convergence time of the permeability as a function of c_s^2 and viscosity for the random 2-D porous media using criteria 2 $|\frac{\partial K(t)}{\partial t}| < 10^{-6}$.

3.4. Application of the TRT to Fontainebleau Sandstone

[38] A 3-D image of a small sample of Fontainebleau sandstone was acquired by an X ray microtomography system using a spatial resolution of $\delta_{res} = 6$ µm (see Figure 8). Segmentation of the acquired gray level image was then performed by thresholding at the minimum between the two peaks of the gray level histogram (details about the image acquisition and processing are given in the work of

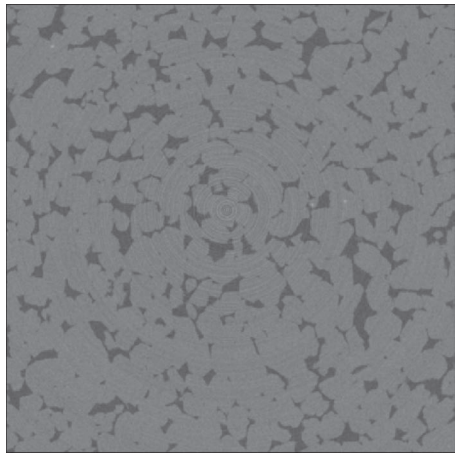

Figure 8. Microtomographic 2-D slice of the Fontainebleau sandstone sample of porosity $\phi = 14.5\%$. The corresponding 3-D image size is 500^3 with a 6 µm voxel size.

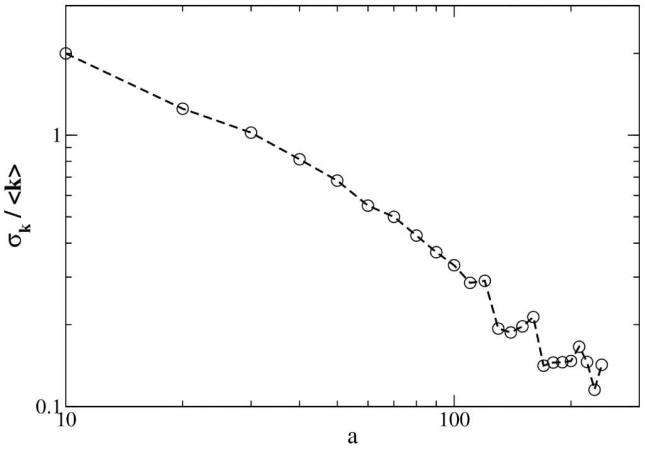

Figure 9. REV size determination of the permeability obtained by the energy dissipation function. Convergence toward the REV, σ_K: standard deviation of $< K(a) >$, a: window size.

Bauer et al. [2011]), resulting in a porosity of 14.5%. The binarized image consists of 500^3 voxels of length 6 µm. This image map is then directly used for LBM simulations using the voxels as the numerical grid. The statistical analysis of the image reveals that the mean grain size of the sandstone is 250 µm. The correlation length of the segmented image was determined by means of the autocorrelation function $A(\vec{h}) = < f(\vec{r}) f(\vec{r} + \vec{h}) >$. The correlation length L was then deduced from an exponential fit applied to the autocorrelation function [*Keehm and Mukerji*, 2004]. We obtained a correlation length of $L = 13$ voxels, which is very close to the mean pore diameter ~ 80 µm (~ 13.33 voxels).

[39] The first issue is to determine if the selected volume of the imaged sample (i.e., 3 mm^3) is sufficiently large to represent a given property of the porous medium. A very efficient way to determine the representative elementary volume (REV) size is, first, to compute the continuum variable—here the permeability—over different averaging windows moved over the sample. Then, REV size and the convergence rate toward the REV can be determined from the variation of $\delta(a) = |\sigma_K(a)/ < K(a) > |$, where σ_K represents the standard deviation of $< K >$, as function of the window size a [*Bauer et al.*, 2008].

[40] In a recent study, *Keehm and Mukerji* [2004] propose to use a sample size of at least $a = 15L$ in order to reduce the spreading of permeability $\sigma_K(a)$ to about 30%. This value is slightly higher than the one we obtained; in our case the spreading becomes lower than 30% for a sample size of $a \sim 100$ (see Figure 9). This difference might be explained by the fact that we used a better resolution to obtain micro-CT images. Also, the REV for the permeability determined by Darcy's law or by the energy dissipation function might not be exactly identical. Yet, the autocorrelation function might be used to give a fast estimation of the size of the REV without the need to solve for the flow field.

[41] Due to the small size of the sample, we were unable to obtain accurate experimental values its permeability. We therefore estimate its value from experimental data obtained for larger samples. Figure 10 shows a set of permeability values of a series of various Fontainebleau sandstones (taken from *Zinszner and Pellerin* [2007]); the data are well adjusted by an exponential fit $K = \alpha(\phi - \beta)^\gamma$ with $\alpha = 2.62$, $\beta = 2.42$, $\gamma = 4.08$ (RMSE=0.31). Using this law, the permeability of a sample of 14.5% porosity is about $764mD \pm 244mD$.

[42] In Figure 11 we present K_D obtained by the TRT scheme ($\nu = 0.4$ and $\nu = 0.2$) and BGK ($\nu \in [0.01; 0.4]$) as a function of Λ for a sample of 300^3 voxels. The upper value of $\Lambda = 1$ was chosen in order to cover the range of the experimental data. According to equation (2.1), for the

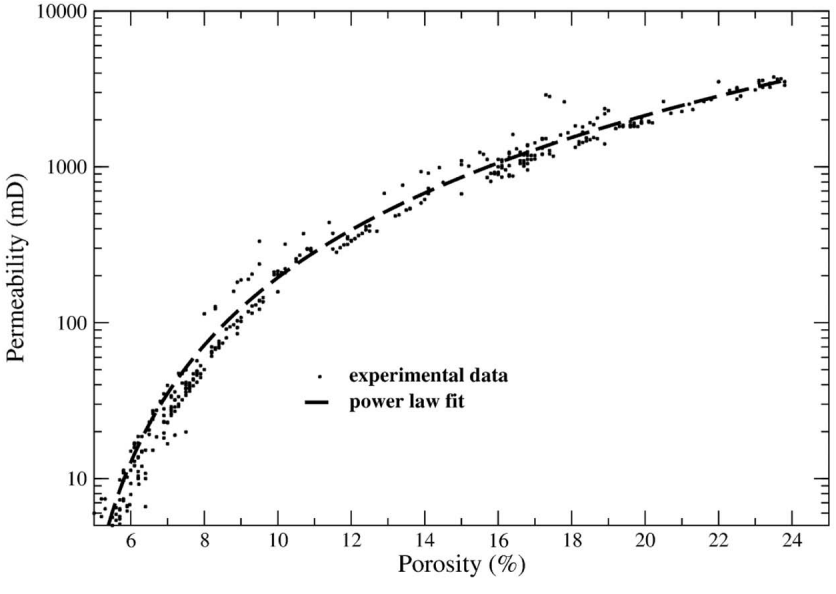

Figure 10. Permeability values of Fontainebleau sandstone samples (data set of *Zinszner and Pellerin* [2007]) as a function of porosity.

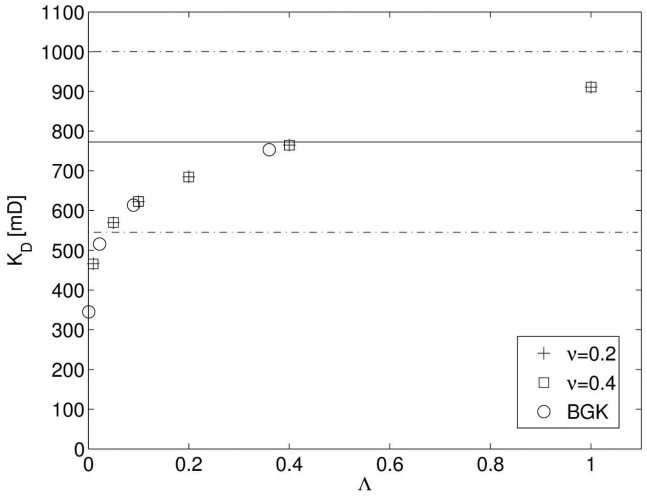

Figure 11. Permeability K_D (given in mD) obtained by TRT and BGK scheme as a function of Λ. The value of Λ for the BGK scheme is deduced from equation (2.1). Driving conditions DC2 were used. Horizontal lines show the range (dashed lines) and the mean (solid line) of the experimental data.

BGK simulations ν was chosen in a way that the range of Λ is similar to the one used for TRT scheme. The given permeabilities are expressed in $[mD]$, conversion from LB units to physical units is done using $K_{phys} = \delta_{res}^2 K_{LB}$. As expected, the permeability values obtained by BGK depend on the viscosity. However, in the investigated domain of ν, permeability values are within the range of the experimental data. Considering the TRT simulations, the nonlinear dependence of K_D on Λ is similar to the one presented in section 3.3. Numerical results are in good accordance with experimental data for $\Lambda \in [0.05; 1]$. As discussed previously this range depends on the image resolution. However, considering theoretical values of Λ providing exact solutions of straight ($\Lambda = 3/16$ or $\Lambda = 1/8$ when accounting for the error of the numerical integration) or diagonal ($\Lambda = 3/8$) Poiseuille flow, we find that for homogeneous structures, permeability can be reasonably estimated within the range of experimental data by using $1/8 < \Lambda < 3/8$.

[43] Table 2 shows the convergence time of the Fontainebleau sandstone as a function of the viscosity for $\Lambda = 0.2$. To smooth data a moving average of $N = 50$ was applied before differentiation. Convergence criteria 2 $\left(\frac{\partial K(t)}{\partial t} < 10^{-6}\right)$ was used. In contrast to the 2-D porous media, there is no minimum in convergence time. Convergence time decreases with decreasing viscosity. This is in contrast to results of *Pan et al.* [2006] and *Ginzburg and d'Humières* [2003] for artificial porous structure where convergence time increases for lower viscosity.

Table 2. Convergence Time for Permeability Measurements of the Fontainebleau Sandstone as a Function of the Viscosity for $\Lambda = 0.2$[a]

Viscosity, ν	Convergence Time
0.01	618
0.05	1325
0.1	1747
0.2	2344
0.4	3094

[a]Convergence criteria 2 $\left(\frac{\partial k(t)}{\partial t} < 10^{-6}\right)$ was applied.

4. Conclusion

[44] In summary, the TRT operator in combination with the bounce-back rule is a powerful LBE scheme for permeability computations in 3-D micro-CT images of porous media, provided that the eventual variability of the results with free parameter Λ is carefully controlled.

[45] The major interest of this approach lies in the viscosity independence of the resulting permeability. Thus, it is the most suitable for immiscible two-phase flow simulations.

[46] The obtained solution however depends on Λ. This dependency is the numerical artifact of the scheme which originates, mainly, from the second-order error in the closure relation of the bounce-back rule and, for higher orders, from the structure of its nonequilibrium corrections. The free parameter Λ has thus no physical meaning. We also note that the TRT scheme is the most simple operator able to maintain fixed the specific combinations for all symmetric and antisymmetric collision modes. This guarantees a viscosity independent permeability. It is therefore the most efficient operator for low Reynolds number flow.

[47] The aim of the present work was to apply it to different types of porous media and to evaluate it in terms of parameter dependence, error and convergence time. We would like to conclude the present article with some remarks and recommendations.

[48] Convergence time strongly depends on the applied viscosity, convergence is faster for low viscosities for the majority of the considered tests. Additionally, we stated that for high values of sound speed c_s convergence time decreases and becomes less dependent on viscosity. Thus, the use of low viscosities in combination with high values of sound speed can strongly reduce computation time.

[49] We have shown that driving conditions DC1 (body force) and DC2 (pressure gradient and zero tangential velocity) give similar results. In LB methods, DC1 is easier to implement and minimizes boundary effects. However, it has very high memory consumption. Thus, for large samples, e.g., 3-D micro-CT images, DC2 is more convenient.

[50] The major objective was to determine the dependence of permeability on Λ. As can be seen from equation (21) and equation (18) that variation of K with Λ reduces as L^{-2} with the applied resolution.

[51] Indeed, using a very high resolution permits the reduction of this dependency, as has already been shown by *Narvaez et al.* [2010]. Similar to BGK simulations dependence on ν reduces with increasing resolution. However, especially in 3-D samples, where memory requirements are more important than in 2-D samples, a compromise between best resolution and maximal sample size, should be accepted. Also, best resolution has generally a technical limit. In this case, dependence on Λ cannot be neglected and therefore has to be thoroughly investigated. We have shown, that dependence on Λ is more pronounced for heterogeneous than for homogeneous samples.

[52] Considering Fontainebleau sandstone digital samples of 14.5% porosity imaged at 6 μm resolution, we can state that permeability values obtained by the TRT scheme

are in good accordance with the experimental data for $\Lambda \in [0.05; 1]$. As mentioned in section 3.4, permeability of homogeneous structures can be estimated reasonably well (within the range of the experimental data) by using Λ in the interval $\Lambda \in [1/8; 3/8]$ which are the values of Λ providing exact solutions for straight or diagonal Poiseuille flow. For the BGK scheme, values are within the range of experimental data in viscosity interval we considered. As expected BGK values depend on the viscosity. Considering viscosity values such that $9\nu^2 = \Lambda^2 \in [0.05; 1]$, the permeability values are then found within the experimental interval. In contrast to that, the TRT scheme allows a very large range of viscosities. It is thus suitable to use this scheme when viscosity contrasts are important (e.g., two phase flow, non-Newtonian fluids...). Finally, we can conclude, that dependence on Λ is less important when determining permeability using Darcy's law instead of the energy dissipation function.

Appendix A: Permeability Computation Based On Viscous Energy Dissipation

[53] Stokes equation can be written as follows:

$$0 = -\frac{\partial P}{\partial x_i} + \rho_0 F_i + 2\nu \sum_j \frac{\partial \Delta_{ij}}{\partial x_j}, \tag{A1}$$

where Δ is the deformation rate tensor $\Delta_{ij} = \frac{1}{2}(\frac{\partial j_i}{\partial x_j} + \frac{\partial j_j}{\partial} x_i)$ for incompressible flow.

[54] A scalar product with the flow profile gives then:

$$0 = -\sum_i j_i \frac{\partial P}{\partial x_i} + \sum_i \rho_0 F_i j_i + \nu \sum_{ij} j_i \frac{\partial}{\partial x_j}\left(\frac{\partial j_i}{\partial x_j} + \frac{\partial j_j}{\partial x_i}\right) \tag{A2}$$

and the incompressibility assumption leads to:

$$\begin{aligned} 0 = &-\sum_i \frac{\partial}{\partial x_i}(P j_i) + \sum_i \rho_0 F_i j_i \\ &+ \nu \sum_{ij}\left[\frac{\partial}{\partial x_j}\left(j_i \frac{\partial j_i}{\partial x_j} + j_i \frac{\partial j_j}{\partial x_i}\right) - \left(\frac{\partial j_i}{\partial x_j}\frac{\partial j_i}{\partial x_j} + \frac{\partial j_i}{\partial x_j}\frac{\partial j_j}{\partial x_i}\right)\right]. \end{aligned} \tag{A3}$$

Viscous energy dissipation can be expressed As $e = \frac{2\nu}{\rho_0}\Delta : \Delta = \frac{\nu}{\rho_0}\sum_{ij}\left[\left(\frac{\partial j_i}{\partial x_j}\right)^2 + \frac{\partial j_i}{\partial x_j}\frac{\partial j_j}{\partial x_i}\right]$. Thus, equation (A3) becomes

$$0 = -\sum_i \frac{\partial}{\partial x_i}(P j_i) + \sum_i \rho_0 F_i j_i + 2\nu \sum_{ij} \frac{\partial}{\partial x_j}(j_i \Delta_{ij}) - \rho_0 e \tag{A4}$$

[55] By integrating this expression over the fluid volume Vf of the sample and using the Gauss-Ostrogradsky theorem, we obtain:

$$\begin{aligned} 0 = &-\underbrace{\iint_{\partial V}\sum_i P j_i dS_i}_{(1)} + \underbrace{\rho_0 \iiint_{Vf}\sum_i F_i j_i dV}_{(2)} \\ &+ \underbrace{2\nu \iint_{\partial V}\sum_{ij} j_j \Delta_{ij} dS_i}_{(3)} - \underbrace{\iiint_{Vf}\rho_0 e dV}_{(4)}, \end{aligned} \tag{A5}$$

where ∂V is the fluid boundary and dS_i the ith component of the elementary surface vector directed toward the outside. We note that the two surface integrals (1) and (3) vanish at the fluid-solid interface (because of the no-slip condition) so that only the volume integrals at the boundary domain remain. From this general equation, we will now study the particular cases of the two applied driving conditions.

Appendix B: Pressure Condition (DC1)

[56] In this case, we applied an inlet (P_{in}) and outlet (P_{out}) pressures in the x-direction, additionally, zero tangential velocity u_y is imposed at these boundaries. At the remaining boundaries, no-slip condition is used. The first term in (A5) becomes then

$$\begin{aligned} -\iint_{\partial V}\sum_i P j_i dS_i &= (P_{in} - P_{out})\iint_{\partial V} j_x dS \\ &= (P_{in} - P_{out}) S < j_x > \\ &= \frac{\nu V < j_x >^2}{K_{xx}}, \end{aligned}$$

assuming that Darcy's law (equation (12)) $K_{xx} = -\frac{\nu < j_x(\vec{x}) >}{< \nabla_x P >} = \frac{L\nu < j_x(\vec{x}) >}{P_{in} - P_{out}}$ is valid.

[57] Since the inlet and outlet boundary surfaces are perpendicular to $\vec{e}_x$ and assuming that $j_y = j_z = 0$, the third term in (A5) becomes:

$$2\nu \iint_{\partial V}\sum_{ij} j_j \Delta_{ij} dS_i = 2\nu \iint_{\partial V} j_x \left(\frac{\partial j_x}{\partial x}\right) dS_x \tag{B1}$$

$$= -2\nu \iint_{\partial V} j_x \left(\frac{\partial j_y}{\partial y} + \frac{\partial j_z}{\partial z}\right) dS_x \tag{B2}$$

$$= 0, \tag{B3}$$

where we have used the fact $j_z = j_y = 0$ at the boundary surfaces.

[58] As the body force is zero equation (A5) becomes:

$$\frac{\nu V}{K_{xx}} < j_x >^2 = \iiint_{Vf} \rho_0 e dV \tag{B4}$$

$$\frac{\nu V}{K_{xx}} < j_x >^2 = \iiint_{Vf} 2\nu \Delta : \Delta dV \tag{B5}$$

and

$$K_{xx} = \frac{< j_x >^2}{2 < \Delta : \Delta >}. \tag{B6}$$

Appendix C: Periodic Condition With Uniform Body Force (DC2)

[59] In the case of the periodic condition in a combination with a uniform body force $\left(F_x \vec{e}_x = \frac{\nu j_x}{\rho_0 K_{xx}} \vec{e}_x\right)$, the relation between permeability and the deformation rate tensor is

simpler to prove. The two surface terms in equation (A5) disappear either because of the no-slip condition or because of the periodicity ($\vec{dS}$ changes its orientation at the inlet and outlet).

[60] The second term of equation (A5) takes the form:

$$\rho_0 \iiint_{Vf} \sum_i F_i j_i dV = \rho_0 F_i \iiint_{Vf} j_i dV = \rho_0 F_x V < j_x >$$

$$= \frac{\nu V}{K_{xx}} < j_x >^2$$

thus, identical to Appendix B, we can deduce K_{xx} from equation (A5) as

$$K_{xx} = \frac{< j_x >^2}{2 < \Delta : \Delta >}. \quad \text{(C1)}$$

[61] **Acknowledgment.** L.T. and H.A. would like to acknowledge financial support from ANR *CO_2 COLINER*.

References

Adler, P., C. Jacquin, and J. Quiblier (1990), Flow in simulated porous media, *Int. J. Multiphase Flow*, *16*(4), 691–712.

Arns, C., M. Knackstedt, M. Pinczewski, and W. Lindquist (2001), Accurate estimation of transport properties from microtomographic images, *Geophys. Res. Lett.*, *28*(17), 3361–3364, doi:10.1029/2001GL012987.

Arns, C. H., M. A. Knackstedt, W. V. Pinczewski, and N. S. Martys (2004), Virtual permeametry on microtomographic images, *J. Pet. Sci. Eng.*, *45*(1–2), 41–46, doi:10.1016/j.petrol.2004.05.001.

Auzerais, F. M., J. Dunsmuir, B. B. Ferreol, N. Martys, J. Olson, T. S. Ramakrishnan, D. H. Rothman, and L. M. Schwartz (1996), Transport in sandstone: A study based on three dimensional microtomography, *Geophys. Res. Lett.*, *23*(7), 705–708.

Bauer, B., L. Talon, and A. Ehrlacher (2008), Computation of the equivalent macroscopic permeability tensor of discrete networks with heterogeneous segment length, *ASCE J. Hydraul. Eng.*, *6*, 784–793, doi:10.1061/(ASCE)0733-9429(2008)134:6(784).

Bauer, D., S. Youssef, M. Han, S. Bekri, E. Rosenberg, M. Fleury, and O. Vizika (2011), From computed microtomography images to resistivity index calculations of heterogeneous carbonates using a dual-porosity pore-network approach: Influence of percolation on the electrical transport properties, *Phys. Rev. E*, *84*(1), 011133, doi:10.1103/PhysRevE.84.011133.

Borne, L. (1992), Harmonic stokes flow through periodic porous media: A 3D boundary element method, *J. Comput. Phys.*, *99*, 214–232.

Cancelliere, A., C. Chang, E. Foti, D. H. Rothman, S. Succi (1990), The permeability of a random medium: Comparison of simulation with theory, *Phys. Fluids A*, *12*, 2085–2088.

d'Humières, D., and I. Ginzburg (2009), Viscosity independent numerical errors for lattice Boltzmann models: From recurrence equations to collision numbers, *Comput. Math. Appl.*, *58*(5), 823–840, doi:10.1016/j.camwa.2009.02.008.

d'Humières, D., I. Ginzburg, M. Krafczyk, P. Lallemand, and L.-S. Luo (2002), Multiple–relaxation–time Lattice Boltzmann models in three dimensions, *Philos. Trans. R. Soc. A*, *360*(1792), 437, doi:10.1098/rsta.2001.0955.

Fatt, I. (1956), The network model of porous media, *Pet. Trans. AIME*, *207*, 144–163.

Ginzbourg, I., and P. Adler (1994), Boundary flow condition analysis for the three-dimensional Lattice Boltzmann model, *J. Phys. II*, *4*(2), 191–214, doi:10.1051/jp2:1994123.

Ginzburg, I. (2007), Lattice Boltzmann modeling with discontinuous collision components: Hydrodynamic and advection-diffusion equations, *J. Stat. Phys.*, *126*(1), 157–206, doi:10.1007/s10955-006-9234-4.

Ginzburg, I. (2008), Consistent Lattice Boltzmann schemes for the Brinkman model of porous flow and infinite Chapman-Enskog expansion, *Phys. Rev. E*, *77*, 066704, doi:10.1103/PhysRevE.77.066704.

Ginzburg, I. (2012), Truncation errors, exact and heuristic stability analysis of two-relaxation-times lattice Boltzmann schemes for anisotropic advection diffusion equation, *Commun. Comput. Physics*, *11*, 1439–1502.

Ginzburg, I., and D. d'Humières (2003), Multireflection boundary conditions for lattice Boltzmann models, *Phys. Rev. E*, *68*, 066614.

Ginzburg, I., F. Verhaeghe, and D. d'Humières (2008a), Two-relaxation-time lattice Boltzmann scheme: About parametrization, velocity, pressure and mixed boundary conditions, *Commun. Comput. Phys.*, *3*, 427–478.

Ginzburg, I., F. Verhaeghe, and D. d'Humières (2008b), Study of simple hydrodynamic solutions with the two-relaxation-times Lattice Boltzmann scheme, *Commun. Comput. Phys.*, *3*, 519–581.

Happel, J., and H. Brenner (1983), *Low Reynolds Number Hydrodynamics*, D. Reidel Publ., Hingham, Mass.

Joekar-Niasar, V., and S. M. Hassanizadeh (2011), Effects of fluids properties on non-equilibrium capillarity effects: Dynamic pore-network modeling, *Int. J. Multiphase Flow*, *37*, 198–214.

Keehm, Y., T. Mukerji, and A. Nur (2004), Permeability prediction from thin sections: 3D reconstruction and Lattice-Boltzmann flow simulation, *Geophys. Res. Lett.*, *31*, L04606, doi:10.1029/2003GL018761.

Lallemand, P., and L.-S. Luo (2000), Theory of the lattice Boltzmann method: Dispersion, dissipation, isotropy, Galilean invariance, and stability, *Phys. Rev. E*, *61*(6), 6546–6562, doi:10.1103/PhysRevE.61.6546.

Manwart, C., U. Aaltosalmi, A. Koponen, R. Hilfer, and J. Timonen (2002), Lattice-Boltzmann and finite-difference simulations for the permeability for three-dimensional porous media, *Phys. Rev. E*, *66*, 016702, doi:10.1103/PhysRevE.66.016702.

Mostaghimi, P., B. Bijeljic, and M. J. Blunt (2010), Simulation of flow and dispersion on pore-space images, SPE 135261, presented at SPE Annual Technical Conference and Exhibition, Florence, Italy, SPE, Allen, Tex.

Narvaez, A., T. Zauner, F. Raischel, R. Hilfer, and J. Harting (2010), Quantitative analysis of numerical estimates for the permeability of porous media from lattice-Boltzmann simulations, *J. Stat. Mech.*, *2010*(11), P11026.

Ovaysi, S., and M. Piri (2010), Direct pore-level modeling of incompressible fluid flow in porous media, *J. Comput. Phys.*, *229*(19), 7456–7476, doi:10.1016/j.jcp.2010.06.028.

Pan, C., L.-S. Luo, and C. T. Miller (2006), An evaluation of Lattice Boltzmann schemes for porous medium flow simulation, *Comput. Fluids*, *35*, 898–909.

Qian, Y., D. D'Humières, and P. Lallemand (1992), Lattice BGK models for Navier-Stokes equation, *Europhys. Lett.*, *17*, 479–484, doi:10.1209/0295-5075/17/6/001.

Rothman, D. (1988), Cellular-automaton fluids; A model for flow in porous media, *Geophysics*, *53*(4), 509, doi:10.1190/1.1442482.

Succi, S. (2001), *The Lattice Boltzmann Equation for Fluid Dynamics and Beyond*, Oxford Univ. Press, New York.

Succi, S., E. Foti, and F. Higuera (1989), Three-dimensional flows in complex geometries with the Lattice Boltzmann method, *Europhys. Lett.*, *10*(5), 433.

Sun, Z., R. Logé, and M. Bernacki (2010), 3D finite element model of semi-solid permeability in an equiaxed granular structure, *Comput. Mater. Sci.*, *49*(1), 158–170, doi:10.1016/j.commatsci.2010.04.042.

Talabi, O., S. AlSayari, S. Iglauer, and M. J. Blunt (2009), Pore-scale simulation of nmr response, *J. Petrol. Sci. Eng.*, *67*(3–4), 168–178, doi:10.1016/j.petrol.2009.05.013.

Talon, L., H. Auradou, and A. Hansen (2010), Permeability of self-affine aperture fields, *Phys. Rev. E*, *82*, 046108, doi:10.1103/PhysRevE.82.046108.

Wu, Y.-S., and K. Pruess (1996), *Flow of non-Newtonian fluids in porous media*, chap. 2, pp. 87–184, Elsevier, New York.

Zaretskiy, Y., S. Geiger, K. Sorbie, and M. Förster (2010), Efficient flow and transport simulations in reconstructed 3D pore geometries, *Adv. Water Resour.*, *33*(12), 1508–1516, doi:10.1016/j.advwatres.2010.08.008.

Zhan, X., L. M. Schwartz, M. N. Toksöz, W. C. Smith, and F. D. Morgan (2010), Pore-scale modeling of electrical and fluid transport in berea sandstone, *Geophysics*, *75*(5), F135–F142, doi:10.1190/1.3463704.

Zinszner, B., and F. Pellerin (2007), *A Geoscientist's Guide to Petrophysics*, Technip Editions, Paris, 384 pp.

H. Auradou and L. Talon, Laboratoire FAST, UMR CNRS 7608, Universités Paris VI et Paris XI, Bâtiment 502, Campus Universitaire, 91405 Orsay Cedex, France. (talon@fast.u-psud.fr)

D. Bauer, N. Gland, and S. Youssef, IFP Energies nouvelles, 1 et 4, avenue de Bois Préau, 92852 Rueil-Malmaison Cedex, France.

I. Ginzburg, Antony Regional Centre, HBAN, Cemagref/Irstea, 1 rue Pierre-Gilles de Gennes CS 10030, 92761 Antony Cedex, France.